Available online at www.sciencedirect.com
SCIENCE DIRECT®
International Journal of Heat and Mass Transfer 48 (2005) 2886–2895
International Journal of HEAT and MASS TRANSFER
www.elsevier.com/locate/ijhmt

Geometrical and flow configurations for enhanced microcantilever detection within a fluidic cell

K. Khanafer, K. Vafai *

Mechanical Engineering Department, University of California, Riverside, CA 92521, United States

Received 15 September 2004; received in revised form 19 November 2004

Abstract

This work focuses on studying the effect of the flow conditions and the geometric variation of the microcantilever's supporting system on the microcantilever detection capabilities within a fluidic cell for various pertinent parameters. Such parameters include Reynolds number, height of the fluidic cell, surface reaction constant, and the Schmidt number. The results of this investigation show that the flow direction has a profound effect on the normal velocity across the microcantilever due to the presence of the supporting mechanism. In addition, the effect of the Reynolds number and the Schmidt number are also found to be significant on the species transfer characteristics within the fluidic cell. An interesting situation is presented in the present investigation, which relates to the effect of fluidic cell height on mass transfer. The results show that as the height of the fluidic cell decreases, mass transfer enhances due to an increase in the axial velocity along the microcantilever. Moreover, the normal velocity is found to decrease when decreasing the height of the fluidic cell and consequently minimizing any unfavorable microcantilever deflection. Finally, a correlation for the average mass flux along the microcantilever is obtained for various pertinent geometrical and flow configuration parameters. This work paves the road for researchers in the area microcantilever based biosensors to design efficient microsenor systems that exhibit minimal errors in the measurements.

Keywords: Fluidic cell; Mass transfer; Microcantilever; Surface reaction

1. Introduction

Microcantilever-based biosensors have received considerable attention for the detection of biohazard and chemical substances, in diagnosis of complicated diseases and for genetic analysis. Other applications include infrared radiation detection [1], mass change detection [2,3], photothermal sensors [4], and surface stress detection [5]. Biosensors are characterized by fast responses and high sensitivity [6]. As such, biosensors properly designed can provide fast and accurate detection of pathogens within a short period of time. A collection of miniaturized biosensors can be arranged on a solid substrate to perform many tests at the same time so higher throughput and speed can be achieved. This collection of microarrays is often called a biochip. First applications of microcantilever arrays as tools for biomolecule detection have been illustrated in the field of DNA hybridization detection [2,7]. The superior capabilities

* Corresponding author. Tel.: +1 951 827 2135/909 787 2135; fax: +1 951 827 2899/909 787 2899.
E-mail address: vafai@engr.ucr.edu (K. Vafai).

0017-9310/$ - see front matter © 2005 Elsevier Ltd. All rights reserved.
doi:10.1016/j.ijheatmasstransfer.2004.11.021

Nomenclature

C	dimensionless analyte concentration
C'	analyte concentration (analyte/solution)
D	mass diffusivity of analyte
H	dimensionless fluidic cell thickness, $H = \frac{h}{l_m}$
h	fluidic cell thickness
k_0	surface reaction constant
κ	non-dimensional surface reaction constant $\kappa = \frac{k_0 l_m}{\rho D}$
L	dimensionless fluidic cell length, $L = \frac{l}{l_m}$
l	fluidic cell length
l_b	microcantilever's supporting mechanism length
L_b	non-dimensional microcantilever's supporting mechanism length, $L_b = \frac{l_b}{l_m}$
l_m	length of the microcantilever
P	dimensionless pressure
p	pressure
Pe	Peclet number, $Pe = Sc\,Re$
Re	Reynolds number, $Re = \frac{U_0 l_m}{\upsilon}$
Sc	Schmidt number $Sc = \frac{\upsilon}{D}$
U	dimensionless axial velocity, $U = \frac{u}{U_0}$
U_0	reference velocity
u	dimensional axial velocity
V	dimensionless normal velocity, $V = \frac{v}{U_0}$
v	dimensional normal velocity
X	dimensionless axial coordinate $X = \frac{x}{l_m}$
x	dimensional axial coordinate
Y	dimensionless normal coordinate $Y = \frac{y}{l_m}$
y	normal coordinate
Y_m	dimensionless location of the microcantilever from the wall
y_m	dimensional location of the microcantilever from the wall

Greek symbols

μ	dynamic viscosity
ρ	fluid density
σ	electrical conductance of the fluid
υ	kinematic viscosity

Subscript

in	quantity at the inlet

of the microcantilevers to detect a specific substance below the detection limits of classical methods have been studied in the literature. Fritz et al. [8] conducted a study on the transduction of DNA hybridization and receptor-ligand binding into a direct nanomechanical response of microfabricated cantilevers. The deflection of the microcantilevers was found to provide a true molecular recognition signal. Baller et al. [6] presented quantitative and qualitative detection of analyte vapors using a microcantilever array to observe transduction of physical and chemical processes into nanomechanical motion of the microcantilever. The measurements of surface stress change due to protein adsorption on a cantilever array were shown by Baller et al. [6]. Hansen et al. [9] demonstrated the discrimination of DNA mismatches using simple microcantilever-based optical deflection assay.

Wu et al. [10] used different geometries of microcantilevers to detect two forms of prostate-specific antigen (PSA) over a wide range of concentrations. Hagan et al. [11] examined microcantilever deflections resulting from adsorption and subsequent hybridization of DNA molecules using an empirical potential. The authors in their study found that the dominant contribution to these deflections arises from hydration forces and not conformational entropy or electrostatics. Label-free protein assay based on microcantilevers array was demonstrated by Arntz et al. [12]. This method allowed biomarker proteins to be detected via measurements of surface stress generated by antigen-antibody molecular recognition. Glucose biosensing using an enzyme-coated microcantilever was studied by Subramanian et al. [13]. The enzyme glucose oxide was immobilized on a micromachined silicon cantilever containing a gold coating. Quantifiable deflection of the microcantilevers was observed in the presence of an appropriate analyte. Analysis of the reaction energetics and the expected thermal response of the microcantilever indicated that the deflection was not a result of reaction-generated heat but resulted from surface induced stresses.

Khaled et al. [14] investigated the main causes for the deflection of microcantilevers embedded in micromechanical biodetection systems. The results of this investigation illustrated that oscillating flow conditions are found to produce significant deflections at relatively large frequency of turbulence. Also, bimaterial effects influencing the microcantilever deflections were found to be prominent at a relatively low frequency of turbulence. Yang et al. [15] analyzed the mechanical design and optimization of piezoresistive cantilevers for biosensing applications. They demonstrated that the introduction of stress concentration regions during cantilever fabrication greatly enhances the detection sensitivity through increased surface stress. Recently, Khanafer et al. [16] established the optimized spatial arrangement for an array of aligned microcantilever sensors placed inside a fluidic cell. The authors illustrate that the optimum spacing distance between the microcantilevers decreases as the fluidic cell thickness decreases. They also

found that the location of the microcantilevers from the wall of the fluidic cell plays a significant role on the optimum distance between the microcantilevers. Also, a correlation for the optimum spacing distance between the microcantilevers was obtained for various pertinent parameters.

The objective of the present work is to investigate the effect of different pertinent parameters on the microcantilever detection capabilities within the fluidic cell such as Reynolds number, Schmidt number, height of the fluidic cell, and the surface reaction constant. Flow direction and the geometry of the microcantilever supporting mechanism can affect the measurements taken by the microcantilever or an array of microcantilevers. Different flow directions over the microcantilever will be investigated in order to achieve a flow direction over the microcantilever with minimum flow disturbances. Other important aspects investigated in this work include the effect of the above cited parameters on the binding process. This is achieved through analyzing the mass species transport within the fluidic cell.

2. Mathematical formulation

Consider a two dimensional, steady incompressible flow through a fluidic cell having a length l and thickness h. The physical model and coordinate system for such a fluidic cell is illustrated in Fig. 1. The microcantilever is placed along the centerline of the fluidic cell. The geometry of the fluidic cell and the microcantilever-based microsensor system used in this study is similar to those commonly used as transducers in chemical and biological sensors. The target molecule (analyte) reacts with the receptor at the surface of the microcantilever. It is assumed that the analyte concentration is dilute as such it does not affect the density. The Soret and Duffor effects are assumed to be negligible. The governing equations for the problem under investigation are based on the balance laws for mass and momentum. Taking into account the above-mentioned assumptions, these equations are

$$\frac{\partial u}{\partial x}+\frac{\partial v}{\partial y}=0, \tag{1}$$

$$\rho\left(u\frac{\partial u}{\partial x}+v\frac{\partial u}{\partial y}\right)=-\frac{\partial p}{\partial x}+\mu\left(\frac{\partial^2 u}{\partial x^2}+\frac{\partial^2 u}{\partial y^2}\right), \tag{2}$$

$$\rho\left(u\frac{\partial v}{\partial x}+v\frac{\partial v}{\partial y}\right)=-\frac{\partial p}{\partial x}+\mu\left(\frac{\partial^2 v}{\partial x^2}+\frac{\partial^2 v}{\partial y^2}\right), \tag{3}$$

$$u\frac{\partial C'}{\partial x}+v\frac{\partial C'}{\partial y}=D\left(\frac{\partial^2 C'}{\partial x^2}+\frac{\partial^2 C'}{\partial y^2}\right), \tag{4}$$

where C', u, v, ρ, p, μ, and D are the concentration of the target molecule, axial velocity, normal velocity, fluid density, pressure, average dynamic viscosity and mass diffusivity of the analyte, respectively. These equations can be transformed into non-dimensional equations using the following non-dimensional variables

$$\left.\begin{aligned} &X=\frac{x}{l_{\mathrm{m}}},\quad Y=\frac{y}{l_{\mathrm{m}}},\quad (U,V)=\frac{(u,v)}{U_0},\\ &C=\frac{C'-C'_0}{C'_{\mathrm{in}}-C'_0},\quad P=\frac{pl_{\mathrm{m}}}{\mu U_0}. \end{aligned}\right\} \tag{5}$$

The resulting non-dimensional governing equations are

$$\frac{\partial U}{\partial X}+\frac{\partial V}{\partial Y}=0, \tag{6}$$

$$U\frac{\partial U}{\partial X}+V\frac{\partial U}{\partial Y}=-\frac{1}{Re}\frac{\partial P}{\partial X}+\frac{1}{Re}\left(\frac{\partial^2 U}{\partial X^2}+\frac{\partial^2 U}{\partial Y^2}\right), \tag{7}$$

$$U\frac{\partial V}{\partial X}+V\frac{\partial V}{\partial Y}=-\frac{1}{Re}\frac{\partial P}{\partial Y}+\frac{1}{Re}\left(\frac{\partial^2 V}{\partial X^2}+\frac{\partial^2 V}{\partial Y^2}\right), \tag{8}$$

$$U\frac{\partial C}{\partial X}+V\frac{\partial C}{\partial Y}=\frac{1}{ScRe}\left(\frac{\partial^2 C}{\partial X^2}+\frac{\partial^2 C}{\partial Y^2}\right), \tag{9}$$

where Re and Sc are the Reynolds and Schmidt numbers, respectively. They are defined as

$$Re=\frac{U_0 l_{\mathrm{m}}}{\upsilon}\quad\text{and}\quad Sc=\frac{\upsilon}{D}. \tag{10}$$

In the above equations, l_{m} and υ are the length of the microcantilever and the kinematic viscosity, respectively.

The boundary conditions for the present study can be written as

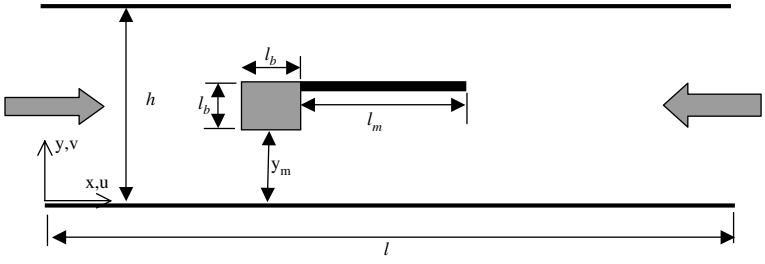

Fig. 1. Physical model and the coordinate system.

1. *Inlet section*

$$X = 0: \quad U = 6\frac{Y}{H}\left(1 - \frac{Y}{H}\right), \quad V = 0 \text{ and } C_{\text{in}} = 1, \tag{11}$$

2. *Outlet section*

$$X = L: \quad \frac{\partial U}{\partial X} = \frac{\partial V}{\partial X} = \frac{\partial C}{\partial X} = 0, \tag{12}$$

3. *Top and bottom walls*

$$Y = 0, H \text{ and } 0 \leqslant X \leqslant L: \quad U = V = \frac{\partial C}{\partial X} = 0, \tag{13}$$

4. *Microcantilever*

The boundary conditions along the microcantilever surface is given by

$$U = V = 0. \tag{14}$$

In this study, it is assumed that the analyte adheres at the surface of the microcantilever at a rate proportional to its concentration at the wall. This is typical for these types of reactions. As such, the reaction at the adhesion surface is balanced by the mass diffusion according to the following relation:

$$\frac{\partial C}{\partial Y} = \kappa C_{\text{surface}}, \tag{15}$$

where κ is the surface reaction constant.

5. *Microcantilever's support*

The boundary conditions along the microcantilever's supporting mechanism are given by

$$U = V = \frac{\partial C}{\partial n} = 0. \tag{16}$$

The average mass flux along the microcantilever is determined in terms of the Sherwood number as follows:

$$\overline{Sh} = \int_0^1 \frac{\partial C}{\partial Y}\, \mathrm{d}X. \tag{17}$$

3. Numerical scheme

A finite element formulation based on the Galerkin method is employed to solve the governing equations subject to the boundary conditions for the present study. The application of this technique is well described by Taylor and Hood [17] and Gresho et al. [18] and its application is well documented [19]. The highly coupled and non-linear algebraic equations resulting from the discretization of the governing equations are solved using an iterative solution scheme using the segregated solution algorithm. The advantage of using this method is that the global system matrix is decomposed into smaller submatrices and then solved in a sequential manner. This technique results in considerably fewer storage requirements. The conjugate residual scheme is used to solve the symmetric pressure-type equation systems, while the conjugate gradient squared method is used for the non-symmetric advection-diffusion-type equations. A variable grid-size system is implemented in the present investigation especially near the walls and close to the microcantilever to capture the rapid changes in the dependent variables. Extensive numerical experimentation is performed to attain grid-independent results for all the field variables. When the relative change in variables between consecutive iterations was less than 10^{-6}, convergence was assumed to have been achieved.

4. Validation

The present numerical method is benchmarked against the works of Young and Vafai [20,21] for forced convective, incompressible flow in a channel with an array of heated obstacles. Comparison of the streamlines between the present solution and that of Young and Vafai [20] shows excellent agreement as shown in Fig. 2. An additional check on the validity of our continuum model in estimating quantities for applications related to the microsensor systems, a comparison of the friction factor between the present study and that of Park et al. [22] inside a micro-channel for various Reynolds numbers is carried out as shown in Fig. 3. This figure shows an excellent agreement.

5. Results and discussion

Various ranges of pertinent parameters that significantly influence the capabilities of the microcantilever detection are investigated in this study. These parameters include Reynolds number, height of the fluidic cell, geometric size of the microcantilever's supporting system, thickness of the fluidic cell and the Schmidt number. The ranges of these parameters are varied as $0.01 < Re < 2$, $1 < H < 5$, $0.01 < L_{\text{b}} < 0.1$ and $500 < Sc < 2000$.

The effect of the flow direction on the normal velocity distribution along different sections of microcantilever is shown in Figs. 4 and 5 for various Reynolds numbers. Figs. 4 and 5 show that flow direction from leading edge towards the tip of the microcantilever exhibits lower values of normal velocity compared with flow direction from tip to the leading edge of the microcantilever. As such the unfavorable deflection caused by high normal velocity values is expected to be reduced for the flow from the leading edge of the microcantilever. In addition, Fig. 4 shows that as the Reynolds number increases, the normal velocity decreases for the case where the flow is

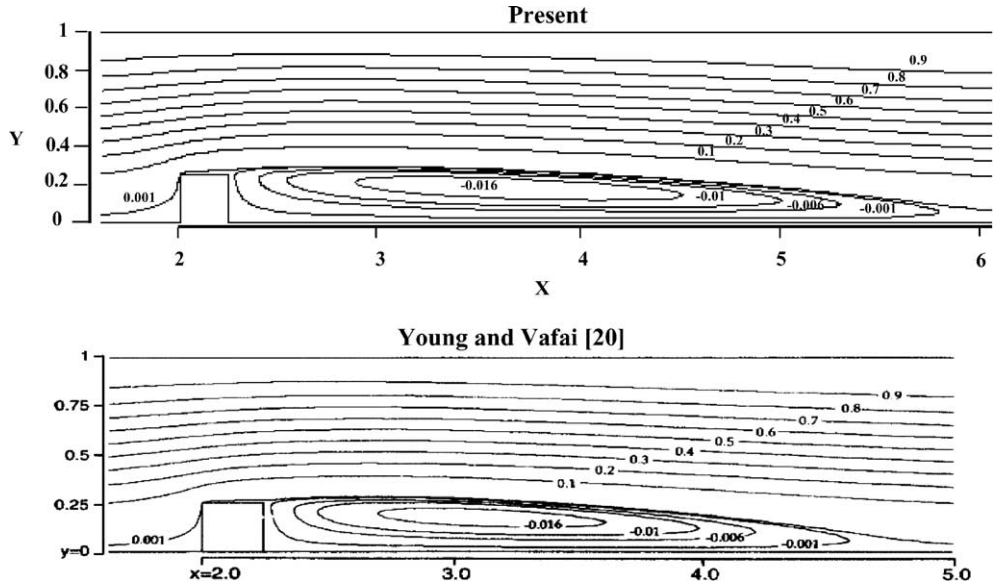

Fig. 2. Comparison of the streamlines contour between the present investigation and that of Young and Vafai [20] (Re = 1000).

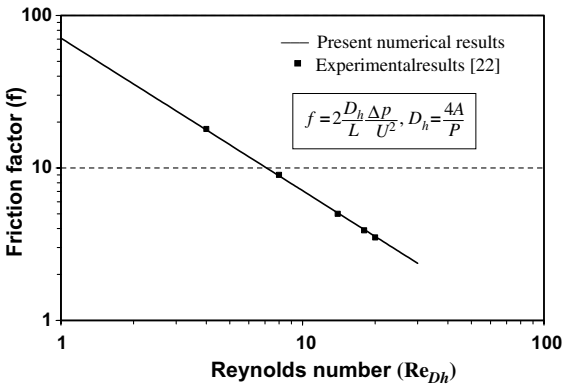

Fig. 3. Comparison of the friction factor between the present study and that of Park et al. [22] for various Reynolds numbers.

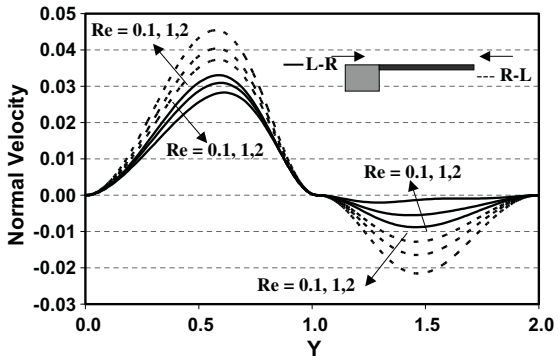

Fig. 4. Effect of the Reynolds number on the normal velocity component along the mid-section of the microcantilever for different flow directions (H = 2, L_b = 0.05).

from left to right towards the tip of the microcantilever. Same characteristic is also observed in Fig. 5 for the normal velocity variation along the tip of the microcantilever. It should be noted that high values of the normal velocity could lead to an increase in the flow disturbances resulting in false readings.

Fig. 6 shows the effect of the surface reaction constant on the normalized concentration of the target molecule along the microcantilever for different flow directions. It can be seen from this figure that the concentration of the target molecule is maximum at the stagnation point and decreases in the direction of the flow over the microcantilever. For the flow direction from the tip of the microcantilever towards the supporting mechanism, the stagnation point is located at the tip where the velocity of the flow is zero and thus concentration of the analyte is greatest. For the second scenario where the flow direction is from the supporting mechanism towards the tip of the microcantilever, the stagnation point is located at the supporting mechanism and accordingly the velocity vanishes. This is associated with the growth of the boundary layer along the microcantilever. As the target molecule deposits on the surface of the microcantilever, the bulk flow is depleted of the target molecules and the bulk concentration decreases in the downstream direction as illustrated in Fig. 6. The effect of the surface reaction rate on the concentration of the target molecule (analyte) is clearly shown in Fig. 6. As the surface reaction rate increases for both flow directions, the target molecule concentration decreases

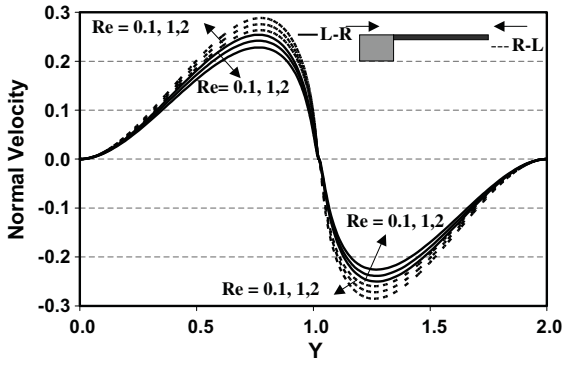

Fig. 5. Effect of the Reynolds number on the normal velocity component along the tip of the microcantilever for different flow directions ($H = 2$, $L_b = 0.05$).

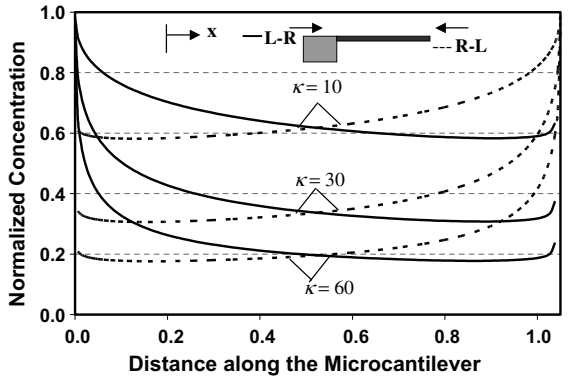

Fig. 6. Comparison of the normalized concentration along the microcantilever for various constant reaction rates and different flow directions ($Re = 2$, $H = 2$, $L_b = 0.05$, $Sc = 800$).

along the surface of the microcantilever. This is because larger amounts of target molecule are deposited on the surface as a result of higher surface reaction rate. Thus, the bulk flow is depleted faster of the analyte.

Fig. 7 demonstrates the effect of the surface reaction rate on the non-dimensional species flux along the microcantilever for different flow direction. It is seen in this figure that the maximum non-dimensional analyte flux occurs at the entry point for both cases and then decreases along the microcantilever similar to the concentration distribution. Moreover, higher non-dimensional analyte flux is observed for higher surface reaction rate as depicted in Fig. 7. Fig. 7 shows that both flow directions exhibit approximately the same total species flux over the entire surface for each of the surface reaction constants. Therefore, the flow direction has a negligible effect on the total mass transfer.

The effect of the geometry variation of the microcantilever's supporting mechanism on the normal velocity

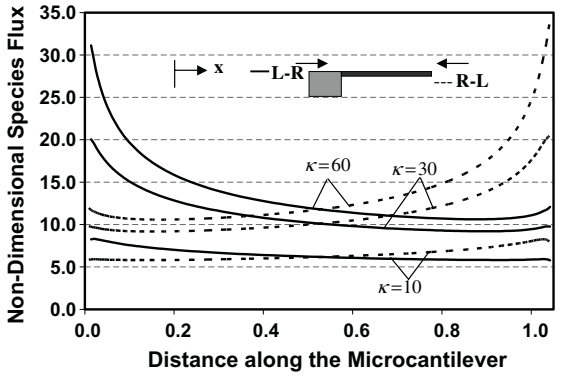

Fig. 7. Comparison of the normalized species flux along the microcantilever for various constant reaction rates and different flow directions ($Re = 2$, $H = 2$, $L_b = 0.05$, $Sc = 800$).

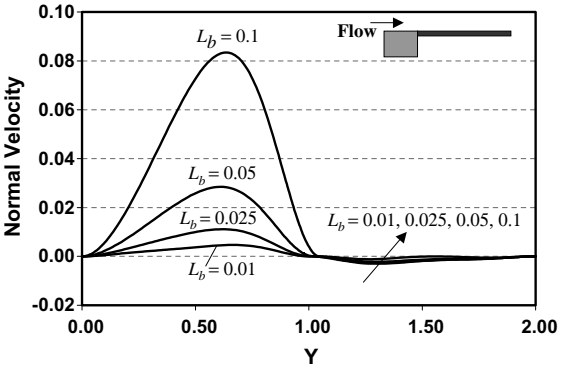

Fig. 8. Effect of the geometry variation of the microcantilever support on the normal velocity component along the mid-section of the microcantilever ($Re = 2$, $H = 2$, $Sc = 800$).

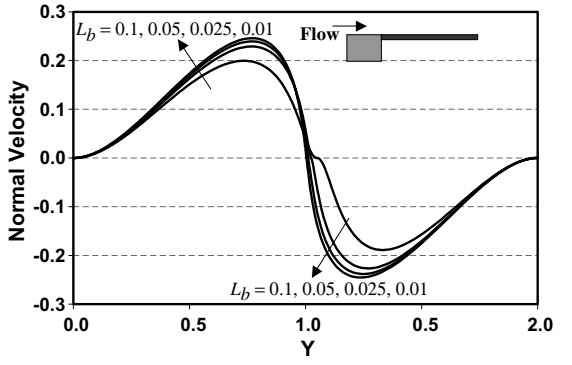

Fig. 9. Effect of the geometry variation of the microcantilever support on the normal velocity component along the tip of the microcantilever ($Re = 2$, $H = 2$, $Sc = 800$).

component at different sections is shown in Figs. 8 and 9. It can be seen in Fig. 8 that as the dimensions of

the support decreases, the magnitude of the normal velocity within the fluidic cell decreases. As such, less flow disturbances are generated due to the presence of the support within the fluidic cell. It should be noted that low normal velocities will bring the target molecules close to the surface of the microcantilever while avoiding creating additional disturbances. Therefore, the size of the microcantilever's support should be an important consideration in the design of the fluidic cell. Fig. 8 shows that the normal velocity is almost symmetric around the tip of the microcantilever and therefore its effect is negligible along the tip of the microcantilever.

Another important parameter that affects the microcantilever detection capabilities is the height of the fluidic cell. Figs. 10 and 11 show the effect of varying the height of the fluidic cell on the normalized concentration and non-dimensional target molecule flux. An interesting scenario is observed in Figs. 10 and 11. It is seen in Fig. 11 that as the height of the fluidic cell decreases, the mass flux (or deposition rate) on the microcantilever increases. This is associated with a high axial velocity along the microcantilever at small fluidic cell heights. This is due to the presence of the supporting system, which produces a profound nozzle effect at small fluidic cell thicknesses. Also, as the fluidic cell height decreases, the mass transfer increases. However, at a larger fluidic cell height, the effect of the presence of the supporting system is quite small on the axial velocity where the nozzle effect is negligible. This is confirmed in Figs. 12 and 13, which illustrate the variation of the axial velocity at various locations for different fluidic cell heights. Fluidic cell height of $H = 1$, exhibits higher axial velocity which translates into higher species flux.

Fig. 14 shows the velocity contours for various fluidic cell heights. The effect of the presence of the supporting system on the flow characteristics over the microcantilever is clearly evident for $H = 1$. As the fluidic cell height increases, the maximum axial velocity decreases within the fluidic cell. In addition, the effect of decreasing the

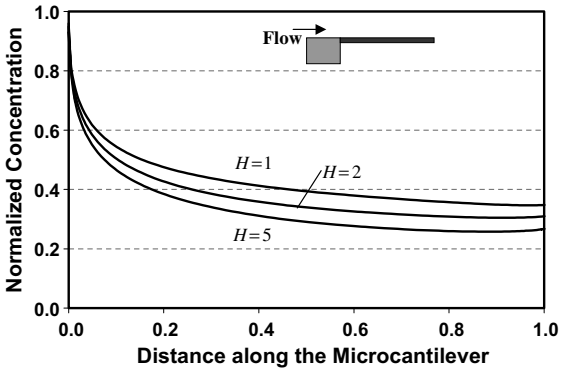

Fig. 10. Normalized concentration along the microcantilever for various fluidic cell heights ($Re = 2$, $\kappa = 30$, $L_b = 0.05$, $Sc = 800$).

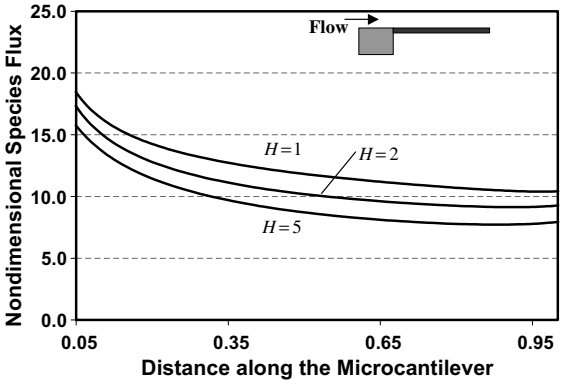

Fig. 11. Normalized species flux along the microcantilever for various fluidic cell heights ($Re = 2$, $\kappa = 30$, $L_b = 0.05$, $Sc = 800$).

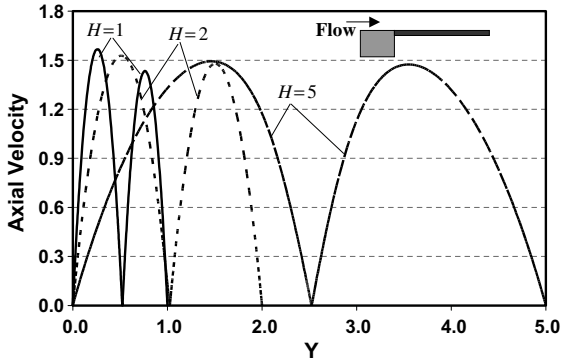

Fig. 12. Effect of the fluidic cell height on the axial velocity along the mid-section of the microcantilever ($Re = 2$, $\kappa = 30$, $L_b = 0.05$, $Sc = 800$).

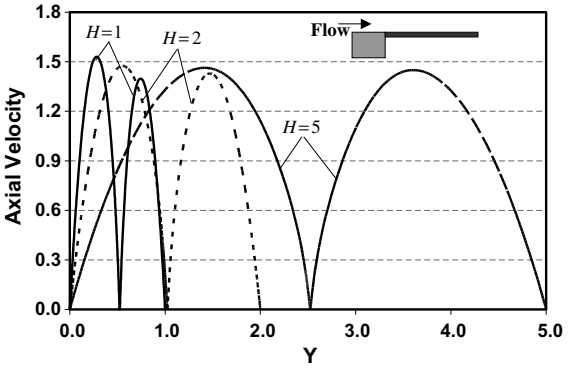

Fig. 13. Effect of the fluidic cell height on the axial velocity along the tip-section of the microcantilever ($Re = 2$, $\kappa = 30$, $L_b = 0.05$, $Sc = 800$).

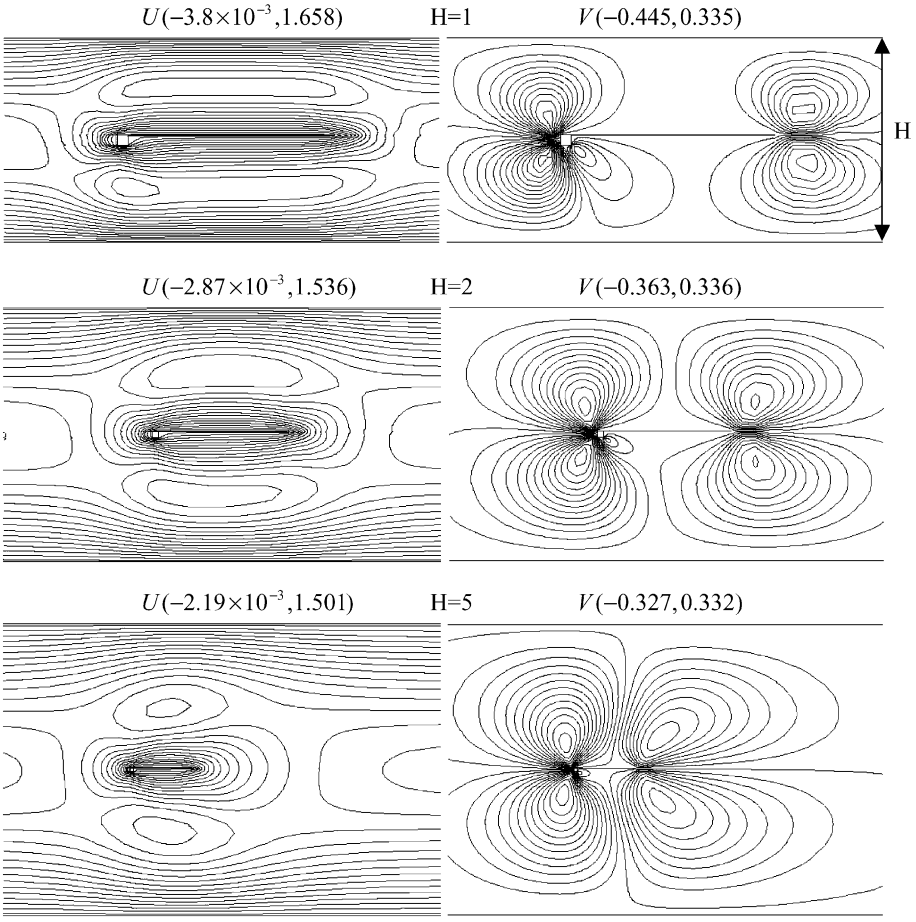

Fig. 14. Velocity contours for various fluidic cell heights ($Re = 2$, $k_0 = 30$, $L_b = 0.05$).

height of the fluidic cell on the normal velocity is also demonstrated in Fig. 14. The maximum normal velocity within the cell decreases with an increase in the height of the fluidic cell. Thus, it is beneficial to have a fluidic cell with a smaller thickness so that the flow disturbances are minimized. Symmetry condition exists in the velocity contours about the centerline of the fluidic cell as seen in Fig. 14.

The effect of the Schmidt number on the normalized concentration and species flux is shown in Figs. 15 and 16. Schmidt number is defined as the ratio of the fluid kinematic viscosity to the species diffusivity. As the Schmidt number increases, the species boundary layer thickness decreases resulting in mass transfer enhancement within the fluidic cell. As such, the deposition rate of the target molecules on the surface of the microcantilever increases accordingly.

Finally, the effect of varying Reynolds number on the flow concentration and species flux along a microcantilever is shown in Figs. 17 and 18. Fig. 18 shows that as the Reynolds number increases, the normalized species flux along the microcantilever increases. Therefore, the total mass transfer increases within the fluidic cell. As such the deposition rate is larger at higher Reynolds number due to a thinner boundary layer.

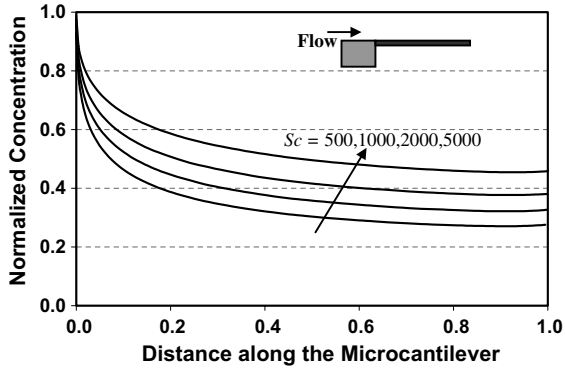

Fig. 15. Normalized concentration along the microcantilever for various Schmidt numbers ($Re = 2$, $\kappa = 30$, $H = 2$, $L_b = 0.05$).

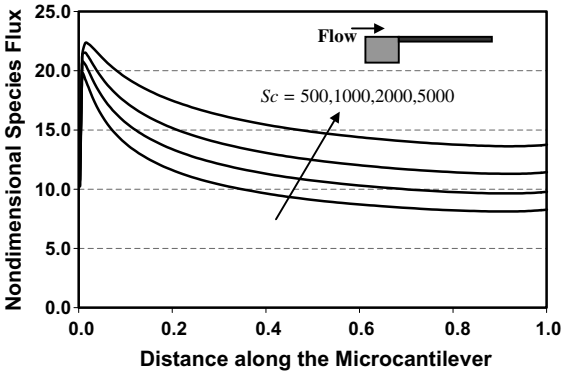

Fig. 16. Normalized species flux along the microcantilever for various Schmidt numbers ($Re = 2$, $\kappa = 30$, $H = 2$, $L_b = 0.05$).

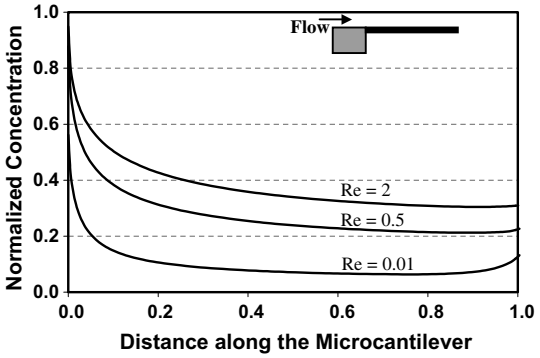

Fig. 17. Normalized concentration along the microcantilever for various Reynolds numbers ($\kappa = 30$, $H = 2$, $L_b = 0.05$, $Sc = 800$).

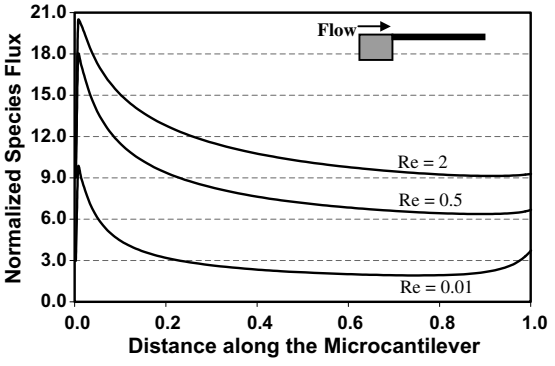

Fig. 18. Normalized species flux along the microcantilever for various Reynolds numbers ($\kappa = 30$, $H = 2$, $L_b = 0.05$, $Sc = 800$).

6. Mass transfer correlation

The variations of the average mass flux (Sherwood number) along the microcantilever is established in terms of the Reynolds number ($0.01 \leqslant Re \leqslant 2$), Peclet number ($8 \leqslant Pe \leqslant 10^4$), surface reaction constant ($10 \leqslant \kappa \leqslant 60$), and the height of the fluidic cell ($1 \leqslant H \leqslant 5$) and presented as the correlation given in Eq. (18).

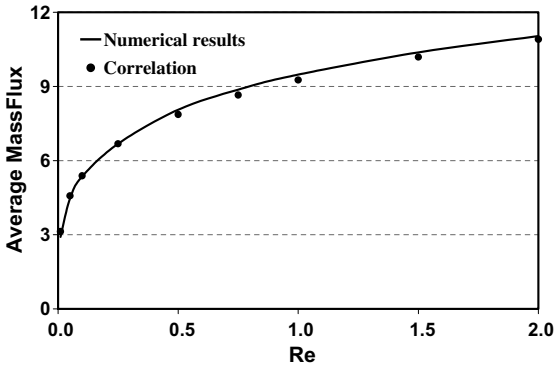

Fig. 19. Comparison of the average mass flux (Sherwood number) between the present numerical results and Eq. (18) for various Reynolds numbers ($Sc = 800$, $H = 2$, $L_b = 0.05$, $\kappa = 30$).

$$\overline{Sh} = 0.7935\,Re^{0.0394}\,Pe^{0.1963}\,\kappa^{0.3703}\,H^{-0.1651}, \tag{18}$$

where the confidence coefficient for the above equation is $R^2 = 99.1\%$. A graphical representation of the above correlation is shown in Fig. 19 for various values of the Reynolds numbers. This figure shows an excellent agreement between the present numerical results and those obtained by the correlation.

7. Conclusions

An investigation of the effect of the flow direction and geometrical variation of a microcantilever's supporting system on the microcantilever detection capabilities is demonstrated in this study based on a comprehensive flow and mass transfer analysis. The governing continuity, momentum and mass transfer equations are non-dimensionalized and solved based on a Galerkin method of weighted residuals. Effects of a wide range of pertinent parameters such as Reynolds number, Schmidt number, surface reaction constant, and the height of the fluidic cell are thoroughly investigated. The results of the present work show that the flow direction has a significant effect on the magnitude of the normal velocity over the microcantilever and consequently the detection capabilities. However, the flow direction is found to have a negligible effect on the total mass transfer within the fluidic cell. The present work demonstrates that as the height of the fluidic cell decreases, the mass transfer within the fluid cell increases while the normal velocity values decrease. Moreover, the results of the present investigation illustrate that geometric size of the microcantilever's supporting system has a

significant role on the microcantilever detection capabilities and establishes the pathway for minimizing the effect of the supporting system. This work is considered very novel since none of approximately 200 papers in the literature have carried any of the optimization and geometrical and flow configurations for enhanced microcantilever detection within a fluidic cell.

Acknowledgment

We acknowledge support of this work by DOD/DARPA/DMEA under grant number DMEA90-02-2-0216.

References

[1] T. Thundat, S.L. Sharp, W.G. Fisher, R.J. Warmack, E.A. Wachter, Micromechanical radiation dosimeter, Appl. Phys. Lett. 66 (1995) 1563–1565.
[2] T. Thundat, R.J. Warmack, G.Y. Chen, D.P. Allison, Thermal and ambient-induced deflections of scanning force microscope cantilevers, Appl. Phys. Lett. 64 (1994) 2894–2896.
[3] T. Thundat, E.A. Wachter, S.L. Sharp, R.J. Warmack, Detection of mercury-vapor using resonating microcantilevers, Appl. Phys. Lett. 66 (1995) 1695–1697.
[4] J. Lai, T. Perazzo, Z. Shi, A. Majumdar, Optimization and performance of high-resolution micro-optomechanical thermal sensors, Sens. Actuat. A: Phys. 58 (1997) 113–119.
[5] G.Y. Chen, T. Thundat, E.A. Wachter, R.J. Warmack, Adsorption-induced surface stress and its effects on resonance frequency of microcantilevers, J. Appl. Phys. 77 (1995) 3618–3622.
[6] M.K. Baller, H.P. Lang, J. Fritz, C. Gerber, J.K. Gimzewski, U. Drechsler, H. Rothuizen, M. Despont, P. Vettiger, F.M. Battiston, J.P. Ramseyer, P. Fornaro, E. Meyer, H.-J. Guntherodt, A cantilever array-based artificial nose, Ultramicroscopy 82 (2000) 1–9.
[7] K. Mosbach, B. Danielsson, Enzyme thermistor, Biochim. Biophys. Acta 364 (1974) 140–145.
[8] J. Fritz, M.K. Baller, H.P. Lang, H. Rothuizen, P. Vettiger, E. Meyer, H.-J. Guntherodt, C. Gerber, J.K. Gimzewski, Translating biomolecular recognition into nanomechanics, Science 288 (2000) 316–318.
[9] K.M. Hansen, H.F. Ji, G.H. Wu, R. Datar, R. Cote, A. Majumdar, T. Thundat, Cantilever-based optical deflection assay for discrimination of DNA single-nucleotide mismatches, Anal. Chem. 73 (2001) 1567–1571.
[10] G.H. Wu, R.H. Datar, K.M. Hansen, T. Thundat, R.J. Cote, A. Majumdar, Bioassay of prostate-specific antigen (PSA) using microcantilevers, Nature Biotechnol. 19 (2001) 856–860.
[11] M.F. Hagan, A. Majumdar, A.K. Chakraborty, Nanomechanical forces generated by surface grafted DNA, J. Phys. Chem. B 106 (2002) 10163–10173.
[12] Y. Arntz, J.D. Seelig, H.P. Lang, J. Zhang, P. Hunziker, J.P. Ramseyer, E. Meyer, M. Hegner, C. Gerber, Label-free protein assay based on a nanomechanical cantilever array, Nanotechnology 14 (2003) 86–90.
[13] A. Subramanian, P.I. Oden, S.J. Kennel, K.B. Jacobson, R.J. Warmack, T. Thundat, M.J. Doktycz, Glucose biosensing using an enzyme-coated microcantilever, Appl. Phys. Lett. 81 (2002) 385–387.
[14] A.-R.A. Khaled, K. Vafai, M. Yang, X. Zhang, C.S. Ozkan, Analysis control and augmentation of microcantilever deflections in bio-sensing systems, Sens. Actuat. B: Chem. 94 (2003) 103–115.
[15] M. Yang, X. Zhang, K. Vafai, C.S. Ozkan, High sensitivity piezoresistive cantilever design and optimization for analyte-receptor binding, J. Micromech. Microeng. 13 (2003) 864–872.
[16] K. Khanafer, A.-R.A. Khaled, K. Vafai, Spatial optimization of an array of aligned microcantilever biosensors, J. Micromech. Microeng. 14 (2004) 1328–1336.
[17] C. Taylor, P. Hood, A numerical solution of the Navier–Stokes equations using finite-element technique, Comput. Fluids 1 (1973) 73–89.
[18] P.M. Gresho, R.L. Lee, R.L. Sani, On the time-dependent solution of the incompressible Navier–Stokes equations in two and three dimensions, in: Recent Advances in Numerical Methods in Fluids, Pineridge, Swansea, UK, 1980.
[19] FIDAP Theoretical Manual, Fluid Dynamics International, Evanston, IL, USA, 1990.
[20] T.J. Young, K. Vafai, Convective cooling of a heated obstacle in a channel, Int. J. Heat Mass Transfer 41 (1998) 3131–3148.
[21] T.J. Young, K. Vafai, An experimental investigation of forced convective characteristics of arrays of channel mounted obstacles, ASME J. Heat Transfer 212 (1999) 34–42.
[22] H. Park, J.J. Pak, S.Y. Son, G. Lim, I. Song, Fabrication of a microchannel integrated with inner sensors and the analysis of its laminar characteristics, Sens. Actuat. A 103 (2002) 317–329.